Journal of Materials Chemistry A

PAPER

View Article Online
View Journal | View Issue

Cite this: J. Mater. Chem. A, 2018, 6, 10388

Zeolite-templated nanoporous carbon for high-performance supercapacitors†

Hao Lu,[a] Kyoungsoo Kim,[b] Yonghyun Kwon,[bc] Xiaoming Sun,[a] Ryong Ryoo *[abc] and X. S. Zhao *[a]

Received 26th January 2018
Accepted 28th April 2018

DOI: 10.1039/c8ta00850g

rsc.li/materials-a

Hierarchical porous carbon prepared with calcium-containing nanocrystalline beta zeolite as the template and ethylene as the carbon source at a relatively low carbonization temperature (600 °C) displayed excellent electrocapacitive properties. The presence of both micro/mesopores and surface oxygen-containing groups on the ordered porous structure, along with a high specific surface area (2280 m^2 g^{-1}) and pore volume (1.95 cm^3 g^{-1}) coupled with good wettability towards the electrolyte enabled the carbon to perform well as a supercapacitor electrode. This carbon electrode achieved a specific capacitance of 250 F g^{-1} at a current density of 1 A g^{-1} with 1 M H_2SO_4 as the aqueous electrolyte measured in a three-electrode system. A symmetric capacitor fabricated with the carbon as both electrodes exhibited a specific capacitance of 161 F g^{-1} at a current density of 1 A g^{-1}, and an excellent cycling stability. After being cycled 17 000 times and shelved for another two months, the electrode exhibited a specific capacitance of 246 F g^{-1} at 1 A g^{-1}, 153% of the initial capacitance, and still maintained an excellent cycle stability. Besides, an all-solid-state supercapacitor cell fabricated with this carbon as both electrodes and polyvinyl alcohol/H_2SO_4 gel as the electrolyte displayed an areal specific capacitance of 413 mF cm^{-2} at a current density of 0.25 mA cm^{-2}.

Introduction

Supercapacitors (SCs) are energy storage devices with high power density and long life time.[1–3] Most currently available commercial SCs are fabricated with activated carbon (AC) as both electrodes, delivering a relatively low energy density.[4,5] Alternative electrode materials other than AC have been actively searched for.[6–8]

Hierarchical porous carbons (HPCs) with micropores, mesopores and/or macropores well-organised in three dimensions (3D) are ideal electrode materials for SCs.[9] The micropores provide abundant space for interacting with electrolyte ions. The mesopores and/or macropores function as ion reservoirs and low-resistance ion-transport tunnels, facilitating fast ion transport into and out of micropores.[9–11]

The zeolite template method has been widely used to prepare HPCs.[12–17] In this method, it has been challenging to selectively deposit carbon in zeolite micropores for preparing highly ordered HPCs[18,19] because a carbon precursor tends to deposit on the external surface of the template.[20] Therefore, the structure of currently available HPCs prepared using the template method contains mainly meso/macropores rather than micro/mesopores, which are more desirable in the development of carbon electrode materials for electric double layer capacitors (EDLCs).[21,22]

Recently, we reported the use of nano-sized beta zeolite as the template to prepare HPCs with a micropore–mesopore hierarchy.[23] Subsequently, we demonstrated that microporous carbons with graphene-like pore walls can be readily prepared by using a lanthanum–zeolite template.[24] In this work, we employed calcium-containing nano-sized beta zeolite as the template and ethylene as the carbon precursor to prepare HPCs. In comparison with other samples templated from micro-sized zeolites Y and beta, the nano-sized zeolite beta templated carbon exhibited the best electrocapacitive performance due to the presence of mesopores, which facilitate the ion and electron transport for both EDLC and pseudocapacitance.

Experimental section

Preparation of zeolite-templated carbon

Both zeolites Y (denoted as YZ) and beta (denoted as BZ) were purchased from Tosoh Corp. Nano-sized beta zeolite (denoted as NBZ) was synthesized as described elsewhere.[25] Ethylene was used as the carbon precursor. A zeolite template (YZ or BZ or NBZ) was placed in a vertical fused quartz reactor equipped with a fritted disk (see Fig. S1†). The template was heated to 600 °C under a dry N_2 gas flow. A mixture of ethylene gas, steam and nitrogen was

[a]School of Chemical Engineering, The University of Queensland, St Lucia, Brisbane, QLD 4072, Australia. E-mail: george.zhao@uq.edu.au

[b]Center for Nanomaterials and Chemical Reactions, Institute for Basic Science (IBS), Daejeon 34141, Republic of Korea

[c]Department of Chemistry, KAIST, Daejeon 34141, Republic of Korea. E-mail: rryoo@kaist.ac.kr

† Electronic supplementary information (ESI) available. See DOI: 10.1039/c8ta00850g

then passed through the zeolite bed. After the carbon deposition was completed, the gas flow was switched to dry N_2 and the temperature was increased to 850 °C and maintained at this temperature for 2 h. The template was washed away with a HF/HCl solution. The samples were washed with deionised water to remove residual chemicals and dried at 150 °C for 48 h. Three carbon replicas of YZ, BZ and NBZ were obtained and the samples are denoted as YZC, BZC and NBZC, respectively.

Characterization

X-ray diffraction (XRD) patterns were recorded on a Rigaku Multiplex instrument using Cu Kα radiation (30 kV, 40 mA). Raman spectra were collected using a Raman spectrometer (Renishaw) with a 514 nm laser. Nitrogen adsorption/desorption isotherms were measured using a Micromeritics Tristar II volumetric adsorption analyzer at liquid N_2 temperature after all samples were degassed at 300 °C for 4 h. Ar sorption isotherms were measured using a Micromeritics ASAP 2020 volumetric adsorption analyzer at liquid Ar temperature. The specific surface area (SSA) of the samples was calculated using the Brunauer–Emmett–Teller (BET) method using data points within a relative pressure range of 0.05–0.2. The total pore volume was estimated at $P/P_0 = 0.95$. The micropore volume was determined by the *t*-plot method. The mesopore size distributions were determined with nitrogen adsorption isotherms using the Barrett–Joyner–Halenda (BJH) model. The micropore size distributions were determined through Ar adsorption isotherms using a quantized liquid density-functional theory (DFT) model, assuming a slit-shaped pore geometry. Scanning electron microscopy (SEM) images were collected on a Verios 460 (FEI) at a landing voltage of 1 kV in deceleration mode (stage bias voltage: 5 kV). Transmission electron microscopy (TEM) images were collected with a Titan E-TEM G2 (FEI) at an acceleration voltage of 300 kV, on a holey carbon grid (300 mesh). X-ray photoelectron spectroscopy (XPS) spectra were acquired by using a Thermo Fisher Scientific Sigma probe with a monochromatic Al Kα X-ray source.

Electrochemical measurements

The working electrodes were prepared by mixing 75 wt% active materials, 20 wt% carbon black as a conductive additive and 5 wt% polytetrafluoro ethylene (PTFE) binder. Then the mixture was pressed onto a stainless-steel mesh and dried at 60 °C for 48 h. A Whatman filter paper (GF/D) was used as the separator. The mass loading of active materials on each current collector was ~2 mg cm^{-2}. Cyclic voltammetry (CV), galvanostatic charge–discharge (GCD) and electrochemical impedance spectroscopy (EIS) measurements were all conducted at room temperature using an Autolab PGSTAT 3020 N.

Electrochemical measurements in an aqueous electrolyte system

The electrolyte was 1 M H_2SO_4 aqueous solution. For the three-electrode system, an Hg/HgO electrode and Ag/AgCl electrode were used as the counter and reference electrodes, respectively. For the two-electrode system, a symmetric SC using the same mass loading (~2 mg) on both electrodes was assembled. CV scans were obtained at various scan rates in the range of 5–200 mV s^{-1}. GCD cycling for the three-electrode and two-electrode systems was performed at current densities ranging from 0.2 to 20 A g^{-1} and 0.1 to 10 A g^{-1}, respectively. EIS measurements were carried out at open circuit potential with an amplitude of 5 mV in the frequency range of 10 mHz to 100 kHz.

Electrochemical measurements of all-solid-state SCs

The polyvinyl alcohol/H_2SO_4 gel electrolyte was prepared as follows:[26] 3 g polyvinyl alcohol (PVA) was added to 30 ml 1 M H_2SO_4 aqueous solution and stirred for 1 h. Subsequently, the mixture was heated to 80 °C under vigorous stirring until the whole solution became clear. Then the working electrodes and separator were soaked with the PVA/H_2SO_4 gel electrolyte and solidified at room temperature for 24 h before they were assembled together. The working electrode had an areal mass loading of ~2 mg cm^{-2} and the active materials had an area of ~1 cm^2. The CV scans of the symmetric all-solid-state cell were obtained at various scan rates in the range of 5–100 mV s^{-1}. The GCD tests were performed at current densities ranging from 0.25 to 20 mA cm^{-2}. The EIS measurements were also conducted in the frequency range of 10 mHz to 100 kHz at an amplitude of 5 mV referring to open circuit potential.

The mass based specific capacitance C_s (in F g^{-1}) measured on a three-electrode system was calculated from the galvanostatic discharge process using the following equation:

$$C_s = I\Delta t/mV \quad (1)$$

The C_s value derived from the GCD data measured on a two-electrode system was calculated from the following equation:

$$C_s = 4I\Delta t/2mV \quad (2)$$

The areal capacitance C_a (in mF cm^{-2}) measured on a two-electrode system was calculated from the following equation:

$$C_a = 4I\Delta t/2SV \quad (3)$$

where, I is the instantaneous current, Δt is the discharge time, m is the mass of the active materials on a single electrode, S is the superficial area of the active materials on a single electrode and V is the potential window.

The volumetric energy density, E_v (in mW h cm^{-3}), and volumetric power density, P_v (in mW cm^{-3}), of an all-solid-state SC were obtained using the following equations:

$$E_v = E/V_{device} \quad (4)$$

$$P_v = 3.6E_v/V_{device} \quad (5)$$

where V_{device} is the volume of the whole device.

Results and discussion

Fig. 1a schematically shows the preparation process of the carbon samples using calcium-containing zeolites as the templates. The SEM images (shown in Fig. 1, and S2†) and TEM

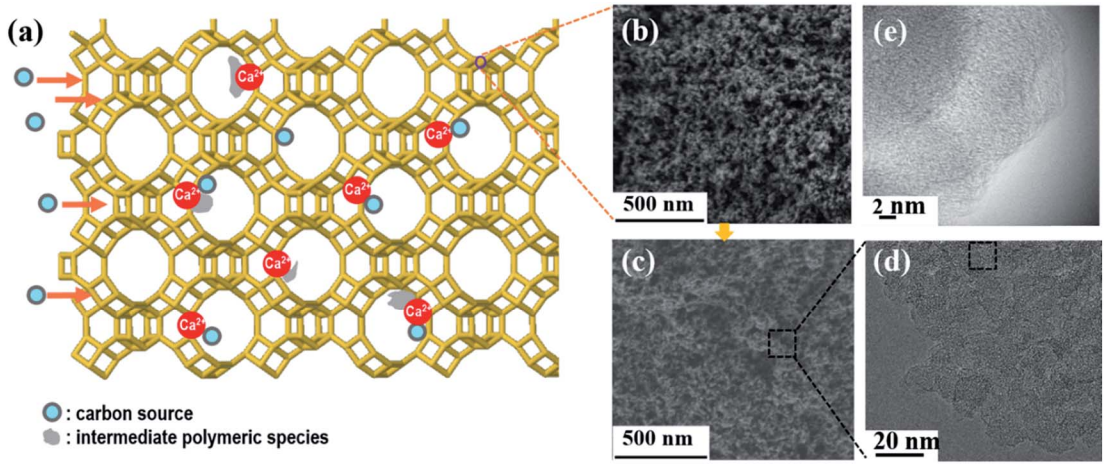

Fig. 1 (a) A schematic diagram showing the process of carbon deposition on calcium-containing zeolite templates; SEM images of (b) template NBZ and (c) resultant carbon replica NBZC; (d) TEM and (e) HRTEM images of NBZC.

images (shown in Fig. 1 and S3†) show that the three samples are good replicas of their separate template. More details about their preparation process and characterisation can be seen in the ESI.† In this paper we will mainly focus on the measurement and interpretation of their electrocapacitive performance.

Firstly, the electrochemical performance was investigated by using CV, GCD and EIS techniques in a three-electrode system with 1 M H_2SO_4 as the aqueous electrolyte at a potential window between −0.3 and 0.7 V *vs.* Ag/AgCl. Fig. 2a shows the CV profiles of the samples measured at a scan rate of 5 mV s^{-1}. All of them exhibit a quasi-rectangular shape with redox peaks due to the pseudocapacitive faradaic reactions of oxygen-containing functional groups, especially NBZC, indicating a better utilisation of oxygen groups on account of a hierarchical porous structure. Besides, the NBZC electrode showed an increased current density compared with the other two electrodes, suggesting a better capacitive performance.[27] Their rate capability is shown in Fig. 2b. The NBZC electrode showed a much better rate capability than YZC and BZC, which is further supported by the EIS results in Fig. 2c. The Nyquist plots show that the NBZC electrode had a much smaller charge resistance than the other two electrodes.

As NBZC showed the best electrocapacitive performance among these three samples, the subsequent investigations were focused on this sample. Fig. 2d and e show the CV and GCD curves of NBZC, respectively. It can be seen that all CV curves exhibit a quasi-rectangular shape while all GCD curves display a quasi-triangular shape, indicating both electric double layer and pseudocapacitive contributions. At a faster scan rate, the CV curve was slightly distorted, implying that some pseudocapacitive species could not participate in the faradaic redox reactions at very fast scan rates.[27] However, the electrode still showed a good rate capability as seen from the data in Fig. 2b and Table S1.† The specific capacitance was 307 F g^{-1} at a current density of 0.2 A g^{-1}, and it remained 177 F g^{-1} at a current density of 20 A g^{-1}.

Fig. 3a shows the N_2 adsorption/desorption isotherms of NBZC. The presence of a hysteresis loop indicates the existence of mesopores. The textual properties of the three samples are compared in Table 1. All three samples have a SSA higher than 2200 m^2 g^{-1}. In comparison with other two samples, NBZC possesses the highest pore volume (1.95 cm^3 g^{-1}) and lowest ratio of micropore volume to total pore volume, indicating a significant contribution of mesopores to the total pore volume. Fig. 3b and c show the well-controlled pore size distribution of NBZC calculated from the DFT model and BJH model, respectively. They exhibit prominent micropore and

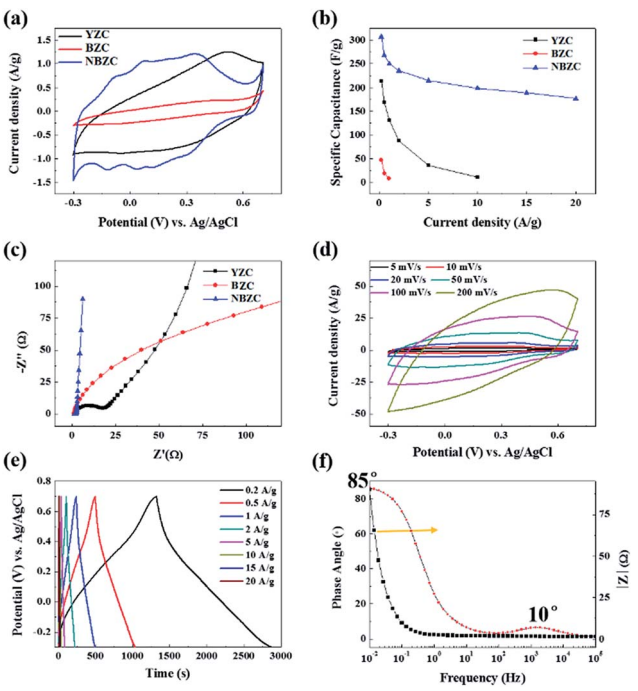

Fig. 2 Electrocapacitive properties of different electrode materials measured using a three-electrode system with 1 M H_2SO_4 as the aqueous electrolyte: (a) CV curves at a scan rate of 5 mV s^{-1}, (b) rate capability, and (c) EIS curves. (d) CV curves at scan rates ranging from 5 mV s^{-1} to 200 mV s^{-1}, (e) GCD curves at current densities ranging from 0.2 A g^{-1} to 20 A g^{-1}, and (f) Bode plots of the NBZC electrode.

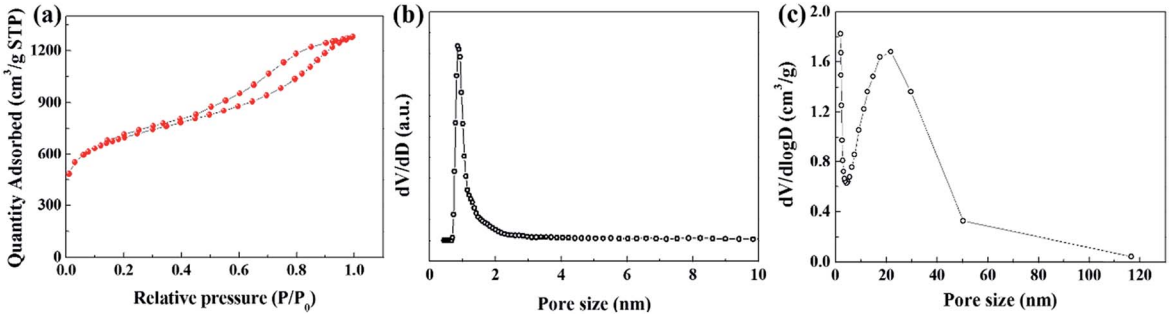

Fig. 3 N_2 adsorption/desorption isotherms (a) and pore size distribution curves calculated using the DFT model (b) and BJH model (c).

Table 1 Textual properties of the samples[a]

Sample	S_{BET} ($m^2\ g^{-1}$)	V_{total} ($cm^3\ g^{-1}$)	V_{micro} ($cm^3\ g^{-1}$)	V_{micro}/V_{total} (%)
YZC	2220	1.12	0.89	79.5
BZC	2770	1.39	0.91	65.5
NBZC	2280	1.95	0.65	33.3

[a] S_{BET}: the specific surface area from BET. V_{total} ($cm^3\ g^{-1}$): total pore volume estimated at $P/P_0 = 0.95$. V_{micro}: volume of micropores calculated by the *t*-plot method.

mesopore peaks centred at 1 nm and 20 nm, respectively. The micropores provide sufficient active sites for EDLC and the mesopores enable active ions in the micropores to have nanometre transport distances.[9,28–31] In comparison, as shown in Fig. S6,† YZC and BZC only exhibit a prominent micropore peak centred at 1 nm, which leads to a larger charge resistance and electrolyte diffusion resistance and thus an ordinary rate capability. Moreover, compared with chemical activation, the zeolite template method can afford a more ordered straight hierarchical porous structure. This enables the NBZC carbon electrode to have low-resistance ion-transport paths, as shown in the Nyquist plots in Fig. 2c and S5,† which is beneficial for both the rate capability and power density.[2,32,33]

Furthermore, the good wettability of NBZC benefitting from a certain degree of graphitization further enhances the ion transfer efficiency.[29] The HRTEM image in Fig. 2e shows a certain degree of graphitization of NBZC which is consistent with the Raman spectroscopy results in Fig. S7,† showing a much higher intensity of the G-band than that of the D-band. This is beneficial for the surface wettability as well as the electronic conductivity of NBZC as the electrode.[34]

Fig. 4a and S8a† shows the XPS survey spectra of the three samples. The quantitative analysis showed that they contained a similar content of oxygen – 9.9 at%, 10.6 at%, 9.2 at%, respectively. But as can be seen from the CV profiles in Fig. 2a, the oxygen functional groups of NBZC were better utilised. This may be because of the well-organised hierarchical porous structure, which enables the electrolyte ions to have more sufficient interaction with the oxygen groups evenly spreading on the carbon NBZC, supported by Fig. S9.† In summary, the excellent performance of NBZC is on account of the ordered straight hierarchical porous structure originating from the zeolite template method and pseudocapacitance contribution from the evenly spread oxygen-containing surface groups on it, as well as the good wettability towards the electrolyte.

The electrochemical performance of the NBZC electrode was further assessed in a symmetric cell with 1 M H_2SO_4 as the aqueous electrolyte. As shown in Fig. 5a, the CV curves exhibit a quasi-rectangular shape, characteristic of a combined contribution of EDLC and pseudocapacitance.[34] And the CV curve only shows limited distortion at a high scan rate of 200 mV s^{-1}, indicating a good rate capability of the cell. Fig. 5b shows the GCD curves of this cell at different current densities ranging from 0.1 A g^{-1} to 10 A g^{-1}. All these curves exhibit a quasi-linear shape demonstrating both EDLC and pseudocapacitance, consistent with the CV test results. The cell electrode exhibited a specific capacitance of 170 F g^{-1} at 0.1 A g^{-1}. Fig. 5c shows the rate capability of the symmetric cell. The capacitance at a high current density of 10 A g^{-1} remained approximately 60% of the value at 0.1 A g^{-1}. Comparisons of the preparation and structural and

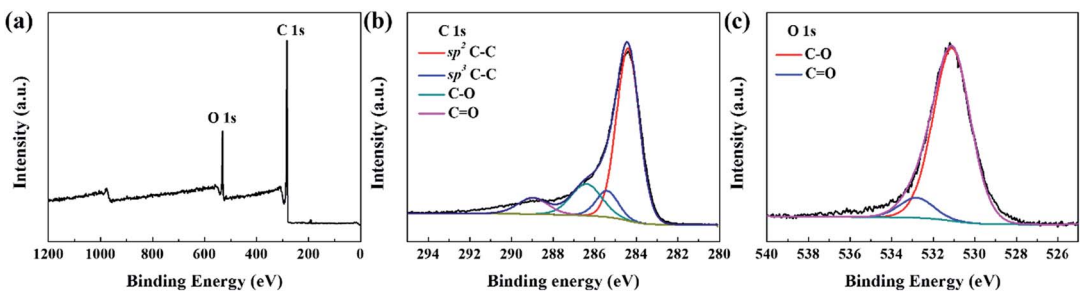

Fig. 4 XPS survey spectra of NBZC (a), and the deconvoluted C 1s (b) and O 1s (c) spectra.

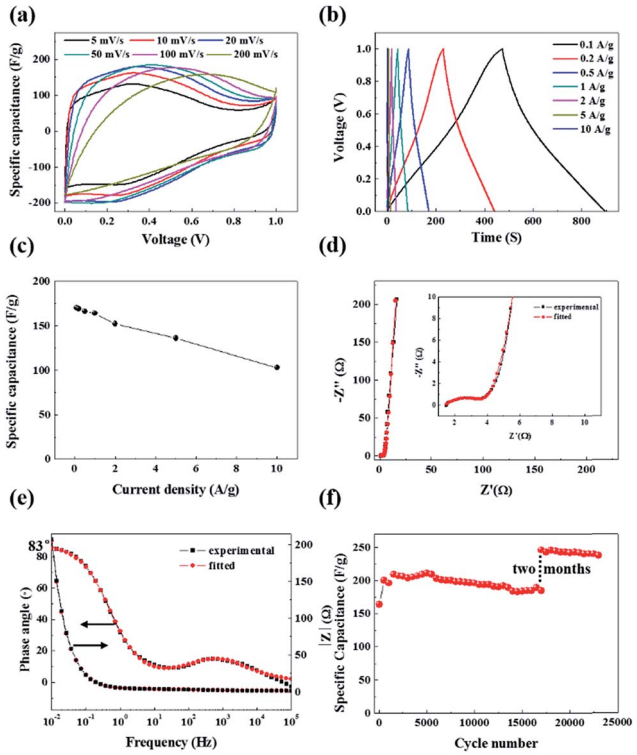

Fig. 5 Electrocapacitive performance of the NBZC electrode in a symmetric cell with 1 M H_2SO_4 as the aqueous electrolyte: (a) CV curves at scan rates from 5 mV s^{-1} to 200 mV s^{-1}, (b) GCD curves at current densities from 0.1 A g^{-1} to 10 A g^{-1}, (c) rate capability, (d) Nyquist plot, (e) Bode plots, and (f) cycling stability at 1 A g^{-1}.

electrocapacitive properties of NBZC with those of other HPCs reported recently are shown in Table. S2.†

Fig. 5d shows the Nyquist plot of the cell. It consists of a semicircle in the high-frequency region and an almost vertical line in the low-frequency region. The almost vertical line in the low-frequency region reveals that EDLC is the dominant capacitance contribution of the cell, consistent with both CV and GCD results. The equivalent circuit shown in Fig. S10† was used to simulate the impedance response of the cell.[35–38] R_s stands for the combination of the contact resistance, electrolyte resistance and bulk resistance of the electrode. R_{ct} is the resistance caused by charge transfer for both EDLC and pseudocapacitance.[39] The constant phase element Q_{dl} represents a part of the capacitance at the high and medium frequency. Z_w represents the electrolyte diffusion resistance, *i.e.*, Warburg impedance.[37] C_m is the main capacitance at low frequency. R_L is the leakage resistance which is relatively high and usually ignored in the circuit. Fig. 5d and e show that excellent fitting results were obtained for both the Nyquist plot and Bode plots. The Nyquist plot shows that the cell had low-value R_s and R_{ct} of 1.43 Ω and 2.38 Ω, respectively. The relatively low equivalent series resistance, the sum of R_s and R_{ct}, *i.e.*, 3.81 Ω, and short Warburg region benefiting from the ordered hierarchical porous structure and a certain degree of graphitization, enable the cell to show a good rate capability.[39,40] The Bode phase angle plot (Fig. 5e) exhibits two maximum values and a phase angle of 83° in the low frequency region, which further proves the coexistence of EDLC and pseudocapacitance.[41]

Long cycle life is one of the critical factors for the application of SCs. As shown in Fig. 5f, the specific capacitance of this SC electrode showed an apparent increase after a certain number of cycles. The capacitance enhancement was further studied through the EIS technique as shown in Fig. 6 and S11.† The electrode retained approximately 120% of the initial capacitance after 17 000 cycles at the current density of 1 A g^{-1}. The slight capacitance value fluctuation may be associated with the minor temperature variation during the long-term cycling test to some extent.[42–44]

Fig. 6a shows that the cell exhibited similar R_s but much lower R_{ct} and Z_w after certain cycles when the capacitance enhanced. Consistent with Fig. 6a, S11a† also shows that the real part resistance, containing R_s, R_{ct} and Z_w, was much lower. The lower resistance facilitates electron transport and thus enables the cell to exhibit a better electrochemical performance.[45] Fig. 6b presents the real part specific capacitance (C') *vs.* frequency. The C' showed almost no change in region 1 and region 2. But in region 3, the value of C' significantly enhanced. This indicates that the capacitance improvement is due to a more efficient utilisation of micropores, which means a higher electrochemically accessible surface area for the cell. The longer soaking time and certain number of GCD tests enable more micropores, especially the inner-region micropores, to be accessed by sufficient electrolyte, thus providing more electrochemically active sites.[46] Fig. 6c presents the imaginary specific capacitance (C'') *vs.* frequency. The C'' showed a maximum value at a frequency of f_0, defining a time constant of $\tau_0 = 1/f_0$. It can be seen that the τ_0 increased from 3.1 s to 5.7 s. Although the more efficient utilisation of inner-region micropores enhanced the capacitance value, it also increased the relaxation time due to relatively lengthening diffusion pathways for ion transport.[47] Fig. S11b† further confirms the increase of τ_0. Therefore, the cell showed a higher specific capacitance and energy density but meanwhile a reduced power density to some extent.[38,48]

More interestingly, as shown in Fig. 5f, the specific capacitance at the current density of 1 A g^{-1} further increased to 246 F g^{-1}, 153% of the initial value, shelved for another 2 months after the 17 000 cycling tests, and it still maintained an excellent cycle stability. The possible reasons for the superior cycle life of this electrode are as follows: (a) the ordered straight hierarchical porous structure enables an excellent charge transfer and ion transport network[28] and facilitates an efficient use of pseudocapacitance from oxygenated functionalities;[2,14,42,49] (b) a certain graphitization degree, which is also beneficial for the electron and ion transfer;[50] and (c) a relatively higher H^+ concentration after a long time, which might also contribute to the further capacitance increase. In our future work, further research on capacitance enhancement after long-term tests will be conducted.

Fig. 7 shows the electrochemical performance of the NBZC electrode in an all-solid-state cell with PVA/H_2SO_4 gel as the electrolyte. A high areal specific capacitance of 413 mF cm^{-2}

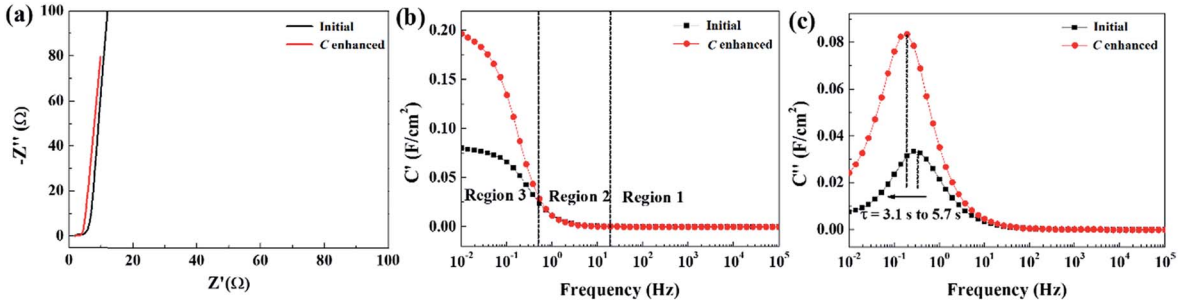

Fig. 6 Nyquist plots (a), real part capacitance (b) and imaginary capacitance (c) *vs.* frequency for the NBZC electrode in a symmetric cell with 1 M H_2SO_4 as the electrolyte.

was obtained at a current density of 0.25 mA cm^{-2}. And it remained at 380 mF cm^{-2}, 246 mF cm^{-2}, and 160 mF cm^{-2} at current densities of 1 mA cm^{-2}, 10 mA cm^{-2}, and 20 mA cm^{-2} respectively. Relatively high volumetric energy density and power density based on the whole device were obtained and three such capacitors connected in series can light a commercial red light-emitting diode (LED, 2.3 V) as shown in Fig. 7d. The all-solid-state cell also exhibited a good cycling stability as shown in Fig. 7e. The areal capacitance value remained around 89% after 3000 cycles at a current density of 5 mA cm^{-2}. Fig. 7f shows the CV curves of the cell at a scan rate of 20 mV s^{-1}. The curves showed no visible change at different bending states, demonstrating its potential as a flexible device.

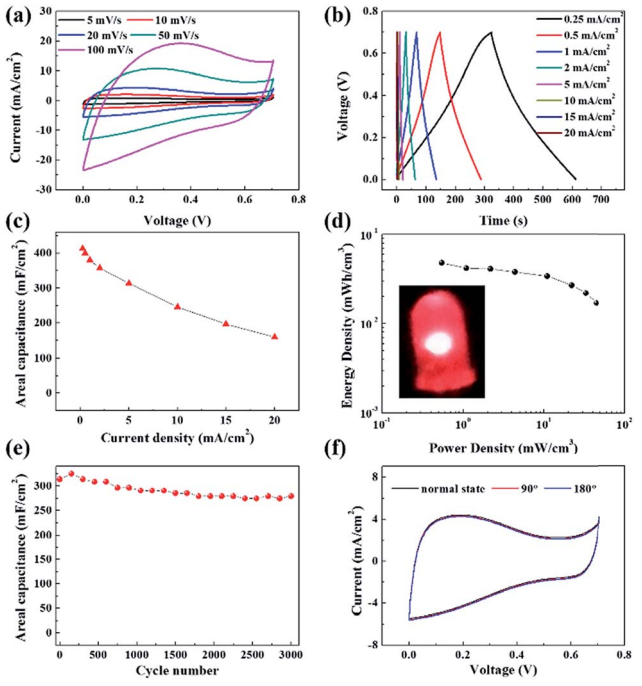

Fig. 7 Electrocapacitive performance of NBZC in an all-solid-state symmetric cell with PVA/H_2SO_4 gel as the electrolyte: (a) CV curves at different scan rates, (b) GCD curves at different current densities, (c) rate capability, (d) a Ragone plot of volumetric energy density *versus* volumetric power density (the inset shows a 2.3 V LED powered by 3 SC cells connected in series), (e) cycling stability at 5 mA cm^{-2}, and (f) CV curves at 20 mV s^{-1} with different bending angles.

Conclusions

With ethylene as the carbon source and calcium-containing nanobeta zeolite as the template, 3D micro/mesoporous carbons of a high specific surface area were prepared at a relatively low carbonization temperature of 600 °C. The Ca^{2+} localized in micropores of the zeolite can strongly interact with ethylene, leading to selective deposition of carbon in pores instead on the external surface of the template. A comparative study of carbons prepared with different zeolite templates indicated that the sample prepared using nanobeta zeolite displayed the best electrocapacitive performance because of its well-controlled hierarchical porous structure and pseudocapacitance contribution from oxygen-containing surface groups evenly spread on it, as well as the good wettability towards the electrolyte. This carbon exhibited an excellent stability against cycling. The carbon electrode was cycled 17 000 times in a symmetric cell with 120% capacity retained. The EIS data indicate that the capacitance improvement is due to a more efficient use of micropores. The long soaking time and a certain number cycling tests enabled more micropores to be accessed by sufficient electrolyte, thus providing more electrochemically active sites. Furthermore, after being shelved for two months after 17 000 cycling tests, this electrode was cycled again at 1 A g^{-1}. The capacitance reached 246 F g^{-1} and it still maintained an excellent cycling stability. The superior cycle life of this carbon is on account of the ordered straight micro-mesopore hierarchy, a certain graphitization degree and the relatively higher H^+ concentration after a long soaking time. More research on further capacitance enhancement after the two-month shelf time is needed in our future work. This carbon also exhibited good performance in an all-solid-state SC with PVA/H_2SO_4 gel as the electrolyte. A high areal specific capacitance of 413 mF cm^{-2} was obtained at a current density of 0.25 mA cm^{-2}. Moreover, the experimental procedure for preparing zeolite-templated carbon can be scaled up as shown in Fig. S1.† With 40 g of zeolite template, about 13 g of carbon can be obtained.

Conflicts of interest

There are no conflicts to declare.

Acknowledgements

The Australian Research Council is acknowledged for supporting this research work (FL170100101). The UQ Vice-Chancellor's Research and Teaching Fellowship Program (2015000144) is also acknowledged. R. R., K. K, and Y. K. acknowledge support from the Institute for Basic Science under grant number IBS-R004. H. L wishes to thank the UQ-CSC program for providing a scholarship.

Notes and references

1 P. Simon and Y. Gogotsi, *Nat. Mater.*, 2008, **7**, 845–854.
2 L. L. Zhang and X. Zhao, *Chem. Soc. Rev.*, 2009, **38**, 2520–2531.
3 P. Simon, Y. Gogotsi and B. Dunn, *Science*, 2014, **343**, 1210–1211.
4 T. Lin, I.-W. Chen, F. Liu, C. Yang, H. Bi, F. Xu and F. Huang, *Science*, 2015, **350**, 1508–1513.
5 L. L. Zhang, Y. Gu and X. Zhao, *J. Mater. Chem. A*, 2013, **1**, 9395–9408.
6 R. R. Salunkhe, Y. H. Lee, K. H. Chang, J. M. Li, P. Simon, J. Tang, N. L. Torad, C. C. Hu and Y. Yamauchi, *Chem.–Eur. J.*, 2014, **20**, 13838–13852.
7 R. R. Salunkhe, J. Tang, N. Kobayashi, J. Kim, Y. Ide, S. Tominaka, J. H. Kim and Y. Yamauchi, *Chem. Sci.*, 2016, **7**, 5704–5713.
8 J. Tang and Y. Yamauchi, *Nat. Chem.*, 2016, **8**, 638.
9 D. W. Wang, F. Li, M. Liu, G. Q. Lu and H. M. Cheng, *Angew. Chem.*, 2008, **120**, 379–382.
10 X. Zheng, J. Luo, W. Lv, D. W. Wang and Q. H. Yang, *Adv. Mater.*, 2015, **27**, 5388–5395.
11 X. Fan, C. Yu, J. Yang, Z. Ling, C. Hu, M. Zhang and J. Qiu, *Adv. Energy Mater.*, 2015, **5**, 14011761.
12 T. Kyotani, T. Nagai, S. Inoue and A. Tomita, *Chem. Mater.*, 1997, **9**, 609–615.
13 C. J. Meyers, S. D. Shah, S. C. Patel, R. M. Sneeringer, C. A. Bessel, N. R. Dollahon, R. A. Leising and E. S. Takeuchi, *J. Phys. Chem. B*, 2001, **105**, 2143–2152.
14 X. S. Zhao, F. Su, Q. Yan, W. Guo, X. Y. Bao, L. Lv and Z. Zhou, *J. Mater. Chem.*, 2006, **16**, 637–648.
15 W. Xia, B. Qiu, D. Xia and R. Zou, *Sci. Rep.*, 2013, **3**, 1935.
16 X. Wen, D. Zhang, T. Yan, J. Zhang and L. Shi, *J. Mater. Chem. A*, 2013, **1**, 12334–12344.
17 X. Y. Chen, C. Chen, Z. J. Zhang and D. H. Xie, *J. Mater. Chem. A*, 2013, **1**, 10903–10911.
18 Z. Li, D. Wu, Y. Liang, R. Fu and K. Matyjaszewski, *J. Am. Chem. Soc.*, 2014, **136**, 4805–4808.
19 H. Nishihara and T. Kyotani, *Adv. Mater.*, 2012, **24**, 4473–4498.
20 H. Xu, Q. Gao, H. Guo and H. Wang, *Microporous Mesoporous Mater.*, 2010, **133**, 106–114.
21 J. Chmiola, G. Yushin, Y. Gogotsi, C. Portet, P. Simon and P.-L. Taberna, *Science*, 2006, **313**, 1760–1763.
22 D. Hulicova-Jurcakova, A. M. Puziy, O. I. Poddubnaya, F. Suárez-García, J. M. Tascón and G. Q. Lu, *J. Am. Chem. Soc.*, 2009, **131**, 5026–5027.
23 K. Kim, M. Choi and R. Ryoo, *Carbon*, 2013, **60**, 175–185.
24 K. Kim, T. Lee, Y. Kwon, Y. Seo, J. Song, J. K. Park, H. Lee, J. Y. Park, H. Ihee and S. J. Cho, *Nature*, 2016, **535**, 131–147.
25 M. Choi, K. Na and R. Ryoo, *Chem. Commun.*, 2009, 2845–2847.
26 X. Lu, M. Yu, G. Wang, Y. Tong and Y. Li, *Energy Environ. Sci.*, 2014, **7**, 2160–2181.
27 Z. Lei, L. Lu and X. S. Zhao, *Energy Environ. Sci.*, 2012, **5**, 6391–6399.
28 H. Lu and X. Zhao, *Sustainable Energy Fuels*, 2017, **1**, 1265–1281.
29 L. Qie, W. Chen, H. Xu, X. Xiong, Y. Jiang, F. Zou, X. Hu, Y. Xin, Z. Zhang and Y. Huang, *Energy Environ. Sci.*, 2013, **6**, 2497–2504.
30 M. Biswal, A. Banerjee, M. Deo and S. Ogale, *Energy Environ. Sci.*, 2013, **6**, 1249–1259.
31 G. Zhang and X. W. D. Lou, *Adv. Mater.*, 2013, **25**, 976–979.
32 H. Jiang, J. Ma and C. Li, *Adv. Mater.*, 2012, **24**, 4197–4202.
33 H. J. Liu, J. Wang, C. X. Wang and Y. Y. Xia, *Adv. Energy Mater.*, 2011, **1**, 1101–1108.
34 H. Lu, X. Sun, R. R. Gaddam, N. A. Kumar and X. S. Zhao, *J. Power Sources*, 2017, **360**, 634–641.
35 C. Masarapu, H. F. Zeng, K. H. Hung and B. Wei, *ACS Nano*, 2009, **3**, 2199–2206.
36 W. Wang, S. Guo, I. Lee, K. Ahmed, J. Zhong, Z. Favors, F. Zaera, M. Ozkan and C. S. Ozkan, *Sci. Rep.*, 2014, **4**, 4452.
37 S. K. Meher and G. R. Rao, *J. Phys. Chem. C*, 2011, **115**, 15646–15654.
38 P. Taberna, P. Simon and J.-F. Fauvarque, *J. Electrochem. Soc.*, 2003, **150**, A292–A300.
39 J. Zhang and X. Zhao, *ChemSusChem*, 2012, **5**, 818–841.
40 A. Di Fabio, A. Giorgi, M. Mastragostino and F. Soavi, *J. Electrochem. Soc.*, 2001, **148**, A845–A850.
41 B. E. Conway, *J. Electrochem. Soc.*, 1991, **138**, 1539–1548.
42 Y. Wang, W. Lai, N. Wang, Z. Jiang, X. Wang, P. Zou, Z. Lin, H. J. Fan, F. Kang and C.-P. Wong, *Energy Environ. Sci.*, 2017, **10**, 941–949.
43 F. Rafik, H. Gualous, R. Gallay, A. Crausaz and A. Berthon, *J. Power Sources*, 2007, **165**, 928–934.
44 S. Dutta, A. Bhaumik and K. C.-W. Wu, *Energy Environ. Sci.*, 2014, **7**, 3574–3592.
45 Y. Deng, C. Liu, T. Yu, F. Liu, F. Zhang, Y. Wan, L. Zhang, C. Wang, B. Tu and P. A. Webley, *Chem. Mater.*, 2007, **19**, 3271–3277.
46 L.-F. Chen, Y. Lu, L. Yu and X. W. D. Lou, *Energy Environ. Sci.*, 2017, **10**, 1777–1783.
47 J. Chmiola, G. Yushin, R. Dash and Y. Gogotsi, *J. Power Sources*, 2006, **158**, 765–772.
48 C. Portet, P. L. Taberna, P. Simon, E. Flahaut and C. Laberty-Robert, *Electrochim. Acta*, 2005, **50**, 4174–4181.
49 C. O. Ania, V. Khomenko, E. Raymundo-Piñero, J. B. Parra and F. Beguin, *Adv. Funct. Mater.*, 2007, **17**, 1828–1836.
50 L. Sun, C. Tian, M. Li, X. Meng, L. Wang, R. Wang, J. Yin and H. Fu, *J. Mater. Chem. A*, 2013, **1**, 6462–6470.

